Examining Star Formation in the Southern HII Region RCW42

SIG-64

Vipin Kumar[1], S. Vig[1], A. Tej[1], S.K. Ghosh[2], D.K. Ojha[2]

[1]Indian Institute of Space Science and Technology, Thiruvananthapuram

[2]Tata Institute of Fundamental Research, Mumbai

Introduction

The formation of massive O and B type stars which are still embedded in their natal molecular clouds, can be observationally understood by studying the HII regions these stars reside in. The ultracompact nature and large electron number densities of HII regions indicate the early evolutionary stages of massive stars. As the stars evolve, the HII regions also change to compact and classical phases [1]. The various stages of the evolution of massive stars can be understood by studying the radio emission from the ionized gas in the HII regions and the infrared emission from the dust in the molecular cloud. In this study, we investigate the star-forming activity in a southern HII region RCW 42 associated with the IRAS source I09227-5146. The interest in this region arises from its highly negative declination which places it very south in the sky. This has led to this source not being studied extensively in any earlier study. It is located at a distance of 5.8 kpc and has a bolometric luminosity of 7 x 10^5 $L_\odot$ [2]. It has a v_{LSR} of 37.0 km/s [2]. Molecular lines of ^{12}CO and ^{13}CO have been detected towards this source [3]. In the current study, we have analysed multiple wavelength bands allowing us to probe different processes in the region. We have studied the ionized gas emission using the radio continuum images at 610 and 1280 MHz. Hierarchical clustering has been detected in the region using the density estimation technique of Parzen windows [4]. Investigation at near and mid-infrared wavelengths allows us to locate the young stellar objects in the region. Studying the region at far-infrared wavelengths enables us to understand the physical properties of the molecular cloud and the dust clumps present in it.

Observations and Archival Data

- Radio observations at 610 and 1280 MHz were obtained from the Giant Metrewave Radio Telescope archive.
- The observations were carried out on 28 Nov 2005 and 14 July 2005 respectively.
- The data reduction was carried out using the NRAO Astronomical Image Processing System (AIPS).
- Data in the JHK bands was obtained from the Two Micron All Sky Survey archive.
- Data at 3.6, 4.5, 5.8 and 8.0 µm was obtained from the Spitzer Heritage Archive.
- Data at 70, 160, 250, 350 and 500 µm was obtained from the Herschel Science Archive.

Radio Continuum Observations

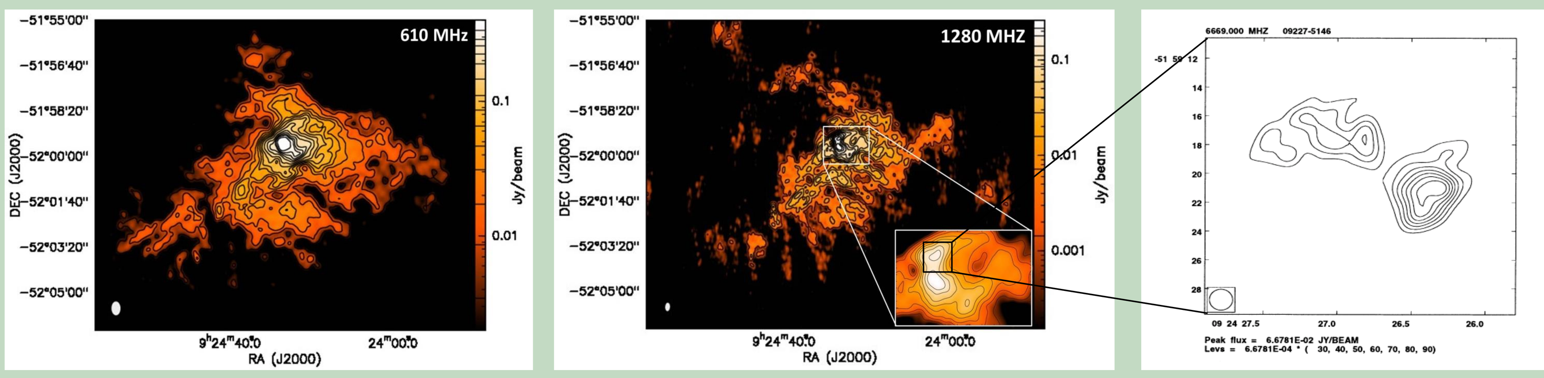

Fig 1 : Radio continuum images at 610 MHz (left), 1280 MHz (middle) and radio continuum contours at 6.67 GHz (right) [5]. Contours are plotted above 3σ and contour levels are marked on the wedges for 610 and 1280 MHz. The x and y axes for the 6.67 GHz image show the RA and DEC J2000 respectively. The beams are shown on the bottom left of each image.

- The complex HII region has similar morphologies at 610 and 1280 MHz.
- It extends by 21.4 x 16.4 and 12.6 x 9.4 pc^2 at 610 and 1280 MHz respectively.
- The continuum at 6.67 GHz has been classified as irregular [5].

Radio continuum characteristics

Frequency (MHz)	Beam size (arcsec^2)	Noise (mJy/beam)	Flux density (Jy) (above 3σ)	Size of HII region (pc^2)
610	10 x 15	0.63	21.9 ± 3.9	21.4 x 16.4
1280	5 x 9	0.49	15.5 ± 2.4	12.6 x 9.4

- Emission measure: $\frac{EM}{cm^{-6}\,pc} = 5.638 \times 10^4 \left(\frac{S}{Jy}\right)\left(\frac{T_e}{10^4 K}\right) b(\nu, Te) \left(\frac{\theta_R^{-2}}{arcmin}\right) = 3.6 \times 10^4\ pc\ cm^{-6}$
- where, $b(\nu, Te) = 1 + 0.3195 \log\left(\frac{T_e}{10^4 K}\right) - 0.213 \log\left(\frac{\nu}{1\ GHz}\right)$
- Electron number density: $n_e = 311.3 \times \left(\frac{S}{Jy}\right)^{0.5} \left(\frac{T_e}{10^4 K}\right)^{0.25} \left(\frac{D}{kpc}\right)^{-0.5} b(\nu, Te)^{-0.5} = 5.3 \times 10^1\ cm$
- Lyman continuum flux: $\left(\frac{N_{Lyc}}{s^{-1}}\right) = \left[\frac{EM}{cm^{-6}\,pc} \times \left(\frac{10^3\,cm^{-3}}{n_e}\right)^{\frac{4}{3}} \times \frac{1}{1.6 \times 10^6} \times (5 \times 10^{49})^{\frac{1}{3}}\right]^3 = 7.3 \times 10^{49}\ s^{-1}$
- Mass of HII gas: $M_{HII} = 80 \times \left(\frac{10^3\,cm^{-3}}{n_e}\right)\left(\frac{N_{Lyc}}{5 \times 10^{49} s^{-1}}\right) M_\odot = 2.2 \times 10^3\ M_\odot$

- S denotes the flux density,
- T_e denotes the electron temperature,
- θ_R denotes the angular radius,
- ν denotes the frequency,
- D denotes the heliocentric distance to the source
- n_e denotes the electron number density. [6]

Cluster Detection at NIR

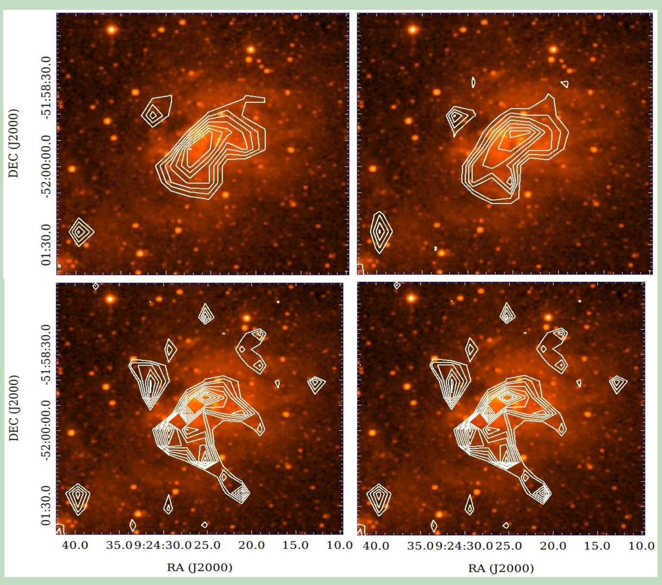

Fig 2. Cluster detection using normal (top) and Gaussian (bottom) windows with a window size of 38″. Square windows are on the right while circular windows are on the left

- Hierarchical clustering is detected in the region using the density estimation method of Parzen windows [4].
- It works on the methodology of identifying an increase in the probability density function.
- The region is divided into multiple windows of square an circular shape.
- A cluster is detected when a window shows a PDF higher than the background threshold.
- Normal windows have equal weightage for all the points in a window while the weightage goes as a Gaussian function from the center for the points in a Gaussian window.
- Gaussian windows are found to be more effective in identifying clusters than normal ones.

Dust Emission

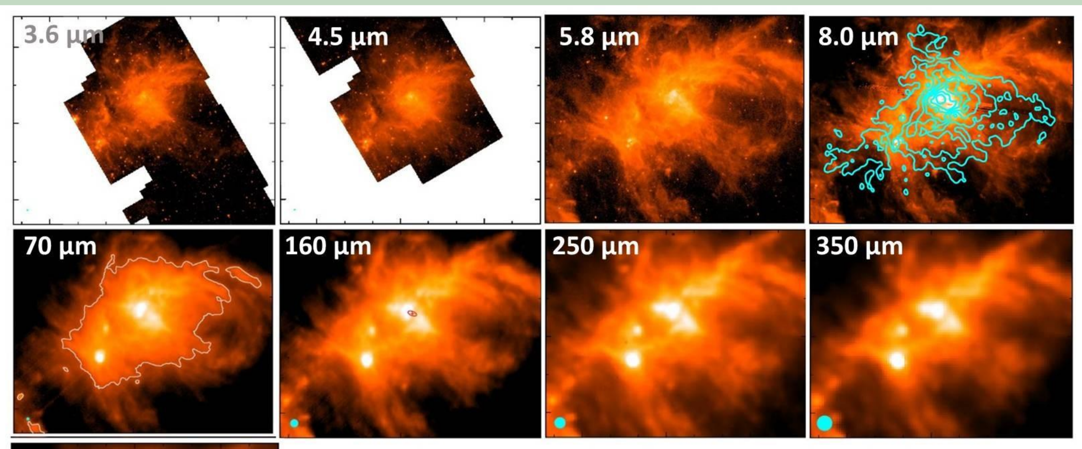

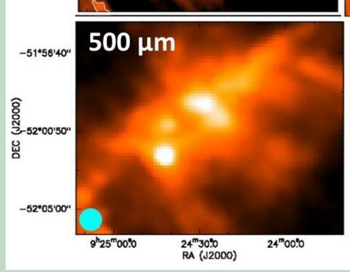

Fig 3. Dust emission towards IRAS 09227-5146 in the four IRAC and five HiGAL bands. The beams are marked on the bottom left in cyan. Radio contours at 610 MHz are overlaid on the 8.0 µm image. The IRAS ellipse and cross are marked on the 160 µm image. The 70 µm image shows the contour at 25σ level, chosen as the molecular cloud's boundary.

- In order to study the dust emission from the region, images taken by the Spitzer Space Telescope at 3.6, 4.5, 5.8 and 8.0 µm and those by the Herschel Space Telescope at 70, 160, 250, 350, 500 µm, were used.
- The Spitzer images show a large number of YSOs and filamentary structures in the region.
- The Herschel images show the cold dust emission and the clumps present in the molecular cloud and have been used to study the cloud's properties.

Column density, Temperature maps and Clumps

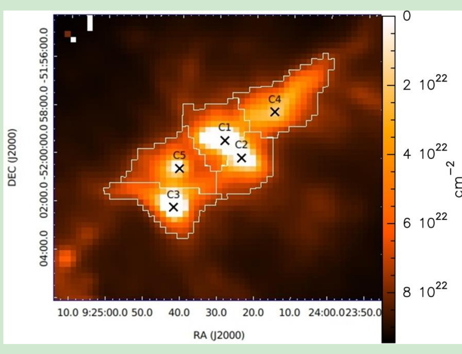

Fig 4. Column density map

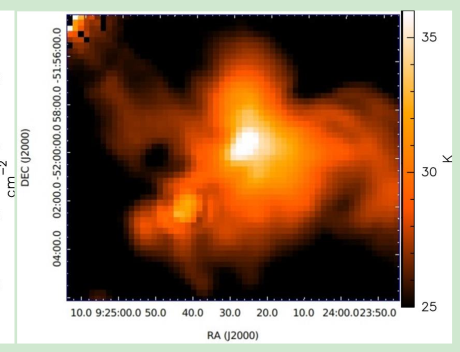

Fig 5. Temperature map

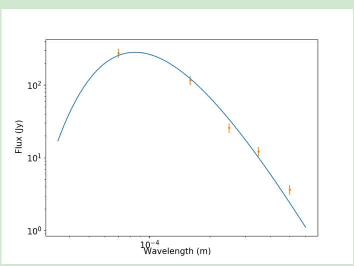

Fig 6. SED for the peak pixel of clump 1

- $F_\nu = \Omega B_\nu(T_D)(1 - e^{-\tau_\nu})$
- $\tau_\nu = m_H \mu N(H_2) k_\nu$
- $k_\nu = 0.1 \left(\frac{\nu}{1000\ GHz}\right)^\beta$

F_ν: flux density at frequency ν
Ω: solid angle subtended;
B_ν: blackbody function;
$m_H\mu$: mean particle mass;
k_ν: dust mass opacity

- Pixel-to-pixel greybody fitting was carried out for the wavelengths 70, 160, 250, 350, 500 µm and maps of column density ($N(H_2)$) and temperature (T_D) are constructed.
- The function used for the fitting [7] is given on the bottom left.
- The value of dust emissivity index, β used for fitting was taken to be equal to 2.
- The peak column density and temperature values are 1.9 x 10^{23} cm^{-2} and 37.6 K respectively.
- The temperatures range from 19.4 – 37.6 K.
- The molecular cloud boundary was chosen as the 25σ level of the 70 µm image.
- Five clumps were identified from the column density map using the CLUMPFIND algorithm
- The clump masses range from 25 x 10^2 $M_\odot$ to 41 x 10^2 $M_\odot$ and the total mass of the molecular cloud is 1.63 x 10^4 $M_\odot$.
- The clump luminosities range from 94 x 10^2 $L_\odot$ to 300 x 10^2 $L_\odot$ and the total luminosity of the molecular cloud is 9.06 x 10^4 $L_\odot$.

Clump Characteristics

Clump	Area (pc^2)	Temperature (K)	Column density (10^{21} cm^{-2})	χ^2_{red}	Mass (10^2 $M_\odot$)	Luminosity (10^2 $L_\odot$)
1	15.05	31.7 ± 1.8	10.7 ± 2.1	0.026	36.77	300.12
2	12.57	31.8 ± 2.0	8.6 ± 1.8	0.050	24.62	204.67
3	15.67	28.4 ± 1.4	11.6 ± 2.1	0.043	41.27	185.05
4	21.25	27.4 ± 1.6	6.8 ± 1.5	0.089	32.87	122.23
5	17.22	26.9 ± 1.5	7.1 ± 1.5	0.081	27.84	94.14

Selection of YSOs using 2MASS

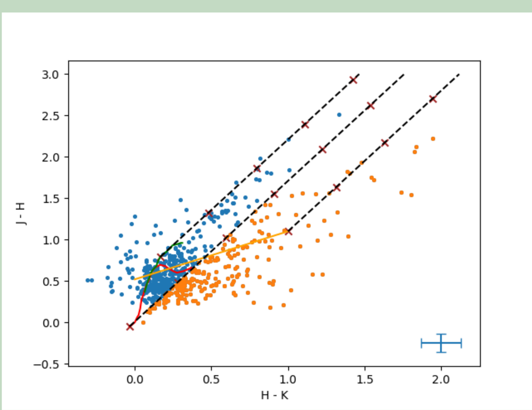

Fig 7. Color-color diagram (J-H vs H-K). Crosses are marked at every A_v = 5

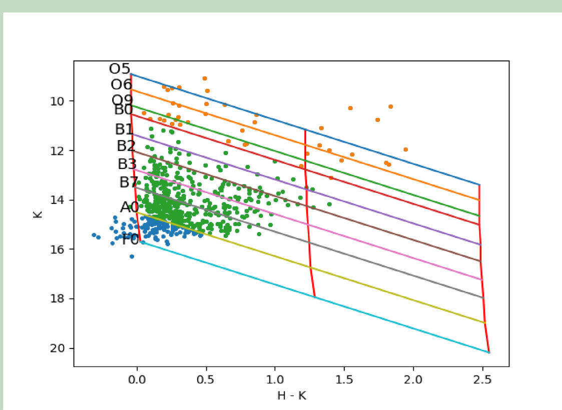

Fig 8. Color-magnitude diagram (K vs H-K). The vertical lines are marked at every A_v = 20

- Young Stellar Objects (YSOs) in the region are identified based on their NIR excess in the color-color diagram.
- The massive O and B type stars responsible for much of the radio emission from the region are identified using the color-magnitude diagram .
- The expanded image of the central region shows that a number of O type stars are present near the radio peak.
- The amount of reddening seen in the identified YSOs is not too high.

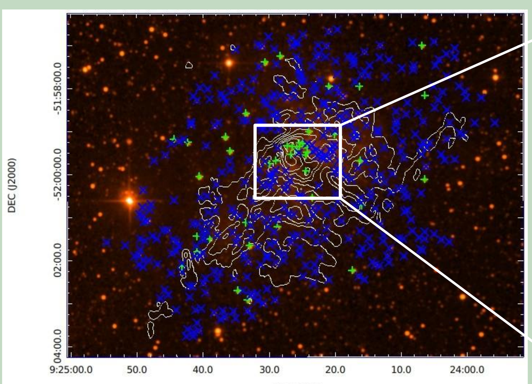

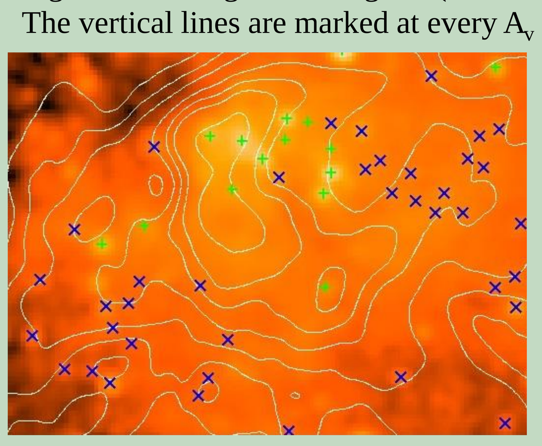

Fig 9. O and B type stars detected in the current study. The O type stars are marked in green and B type in blue. Radio contours at 1280 MHz are overlaid. An expanded image of the central region is also shown.

Conclusion

- The ionized gas emission was observed at 610 and 1280 MHz with flux densities being 21.9 and 15.5 Jy respectively.
- Hierarchical clustering was identified in the region using the density estimation technique of Parzen windows and Gaussian windows were found to be more effective in identifying clusters than normal windows.
- Column density and temperature maps of the region were constructed with the peak values being 1.9 x 10^{23} cm^{-2} and 37.6 K respectively.
- Five clumps were identified from the column density map using the CLUMPFIND algorithm. The clump masses range from 24 x 10^2 to 41 x 10^2 $M_\odot$.
- The radio peak lies close to the peak of Clump 1. Further, C1 also has the maximum luminosity of 300 $L_\odot$ as well as high column density and temperature values of 10.7 x 10^{21} cm^{-2} and 31.7 K respectively.
- Young stellar objects with infrared excess and massive O and B type stars were identified using color-color and color-magnitude diagrams in the near-infrared regime.

References :

1. Garay & Lizano, 1999, PASP, 111(763), 1049
2. Urquhart et al., 2014, MNRAS, 437(2), 1791-1807
3. Wouterloot & Brand, 1999, A & A, 140(2), 177-190
4. Nambiar et al., 2019, MNRAS, 482(3), 3789-3802
5. Walsh et al., 1998, MNRAS, 301(3), 640-698
6. Immer et al., 2012, A & A, 548, A120
7. Gordon, 1987, ApJ, 316, 258-264